Carbon 227 (2024) 119245

Contents lists available at ScienceDirect

Carbon

journal homepage: www.elsevier.com/locate/carbon

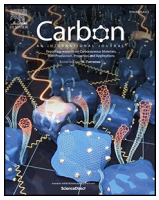

Synchrotron X-ray spectromicroscopy analysis of wear tested graphene-containing alumina coatings

Antonio Mulone [a,*], Plinio Fernandes Borges Silva [a], Hui Yuan [b], Karina Thånell [c], Adam Hitchcock [d], Uta Klement [a]

[a] Chalmers University of Technology, Department of Industrial and Materials Science, Gothenburg, Sweden
[b] McMaster University, Department of Materials Science and Engineering, Hamilton, ON, Canada
[c] MAX IV Laboratory, Lund University, Lund, Sweden
[d] McMaster University, Chemistry & Chemical Biology, Hamilton, ON, Canada

ARTICLE INFO

Keywords:
Synchrotron
STXM
Graphene
Coatings
TEM

ABSTRACT

Thermally sprayed Al_2O_3 coatings containing graphene nano platelets (GNP) have been shown to exhibit improved wear resistance. To understand the positive influence of GNP on wear properties, scanning transmission X-ray microscopy (STXM) analyses were performed to determine the structural and chemical changes that occur on the GNP and alumina matrix after wear tests. STXM results acquired at the C K-edge showed that the GNP are aligned parallel to the specimen surface in the as-sprayed coatings. GNP flakes are also observed at the tribo-surface of the wear tested sample. The results obtained at the Al K-edge show that the aluminum oxide below the wear track becomes amorphous during the wear test and carbon is dissolved in it. Wear tests performed on thermally sprayed pure alumina samples (without GNP) and on sintered bulk alumina prove that neither the presence of GNP nor the porosity in the coating are responsible for the amorphization of the alumina matrix. The results discussed in this work advance the fundamental understanding of graphene-containing composites, which is considered very important to exploit the unique advantages of graphene in technological applications.

1. Introduction

Graphene is an outstanding material that has been extensively studied in the last few years due to its excellent mechanical [1], tribological [2] and corrosion resistance [3] properties. Graphene and its related compounds such as graphene nanoplatelets (GNP) and graphene oxide (GO) are 2D materials: the carbon atoms are connected via strong covalent bonds in a planar hexagonal lattice. In GNP, the 2D graphene sheets are stacked together via weaker van der Waals force. Therefore, thanks to these weaker forces between layers, graphene-related compounds can act as an excellent solid lubricant [4]. Given the beneficial properties of graphene, the research community has recently invested significant efforts in the production of graphene-containing ceramic composites for wear resistant applications [5]. Among the various technologies, suspension plasma spraying (SPS) has proven successful to incorporate graphene in ceramic coatings [6,7]. In SPS, a fine feedstock powder is suspended in a solvent (i.e., generally ethanol or water) [8]. Solvent evaporation during spraying consumes part of the thermal energy, which is an important advantage for the deposition of graphene-containing composites since oxidation of the starting material and graphene degradation is reduced [9]. As previously reported, the addition of limited wt.% of GNP can already lead to a significant increase in the wear resistance of thermally sprayed coatings. For example, as reported by Murrey et al. [10], the addition of 1 wt% of GNP to Al_2O_3 coatings resulted in a two order of magnitude reduction in wear rate and a lower coefficient of friction.

However, despite the advantages mentioned, many key factors need to be considered and optimized to exploit the beneficial properties of graphene in composites. Some can be easily controlled and measured, e.g., the initial wt.% of GNP added to the matrix. However, other factors are more difficult to precisely control and determine, e.g., (i) the resulting wt.% of graphene remaining in the matrix after processing; (ii) the distribution and the orientation of graphene in the host matrix; (iii) the structural changes in the graphene after processing; (iv) the interdependencies between the matrix microstructure and the graphene distribution; among others. To investigate the various key features

* Corresponding author. Chalmers University of Technology, Department of Industrial and Materials Science, Rännvägen 2A, 412 96, Gothenburg, Sweden.
E-mail address: mulone@chalmers.se (A. Mulone).

https://doi.org/10.1016/j.carbon.2024.119245
Received 15 February 2024; Received in revised form 13 May 2024; Accepted 13 May 2024
Available online 13 May 2024

mentioned above, comprehensive characterization analyses are required. In fact, progress in the fundamental understanding of such aspects remains of great importance for the development and industrial implementation of graphene-containing composites. Raman analyses are often performed to confirm that the graphene is retained in the composites and to determine its defectiveness after processing [11] and after wear testing [10]. Image analysis can be performed to estimate the proportion of graphene and its distribution [7]. Transmission electron microscopy (TEM) can be used to determine the in-plane atomic arrangement of graphene [12], whereas scanning electron microscopy (SEM) imaging of fracture surfaces can provide insightful information about the interdependencies between the matrix microstructure and graphene distribution [13]. Although the technologies mentioned above can solve many of the characterization problems related to graphene, new and advanced testing methods are of great interest for the graphene scientific community. For a comprehensive characterization of graphene and graphene-containing composite materials, synchrotron radiation analyses have proven to be at the forefront of graphene research in recent years, [14,15]. Synchrotron radiation offers several advantages: (i) it is well-collimated, (ii) has high brightness, (iii) adjustable energy, and (iv) adjustable polarization [15]. Thanks to such characteristics, synchrotron analyses can provide local information with a high spatial resolution [16], which can be used to reveal structural properties of SPS-deposited alumina and GNP. Synchrotron analyses of graphene and its related compounds can also be used to identify the orientation of the graphene sheets in GNP when applied as a reinforcement in graphene-containing composites. Different orientations of graphene sheets in a host matrix can be detected using polarized X-ray absorption spectroscopy: the graphene anisotropy in a matrix can be measured by enhancement of the C 1s → π* and C 1s → σ* electronic transitions at specific orientations of the sample and the linear polarization direction of the incident X-ray beam [17,18]. In our previous published work, we investigated the feasibility of producing Al_2O_3-GNP coatings as wear resistant coatings by SPS [7]. As shown in that paper, the GNP-containing coating was characterized by a lower coefficient of friction and a lower wear rate compared to the GNP-free alumina coating. The presence of GNP was confirmed by Raman and SEM analysis. However other important information such as the GNP orientation and interaction with the host matrix, as well as the chemical changes that occur due to wear tests, have not been fully revealed.

Scanning Transmission X-ray Microscopy (STXM) is a very powerful synchrotron based spectromicroscopy technique, particularly in the soft X-ray region [19,20]. It provides chemical- and orientation-sensitive imaging based on X-ray absorption near edge fine structure (XANES), also known as near edge X-ray absorption fine structure (NEXAFS) spectroscopy [18]. The spatial resolution is typically 20–40 nm, which is an intermediary spatial resolution between TEM and X-ray microprobe. The data is obtained by measuring images of the sample at each of a sequence of X-ray energies around absorption edges, resulting in a 3D (x, y, E) data set usually called a stack. As the detailed spectral features at an elemental absorption edges are chemically as well as element specific, the stack provides information on the chemical state(s) of the element analyzed. Combining different edges, one can draw a detailed picture of the chemical structure of the analyzed samples [21,22].

In this work, the Al_2O_3-GNP coatings sprayed and tested for wear in our previous study [7] were examined using STXM to determine the structural and chemical changes occurring on the GNP and alumina matrix after wear tests. In addition, the orientation of the GNP in the as-sprayed state and after the wear test was also examined. The results presented here demonstrate the ability of STXM to probe the relationship between the structural and chemical state of graphene and the wear behavior of graphene-containing composites. The progress achieved in fundamental understanding is considered important to exploit the unique advantages of graphene in technological applications.

2. Experimental work

The Al_2O_3-GNP coatings were sprayed using Axial III plasma torch and Nanofeed 350 suspension feeding system from Northwest Mettech Corporation (Mettech, Vancouver, Canada). For the alumina source a water-based powder suspension with 40 wt% solid load was used (obtained from Treibacher Industrie AG, Austria). The GNP content in the water-based suspension was 10 wt%. More experimental details regarding the spraying of the Al_2O_3-GNP coatings are included in our previous work [7]. The Alumina-GNP samples for STXM analysis were prepared using two focused ion beam scanning electron microscopes (FIB-SEM). Lift-outs were made from the surface of the as-sprayed Al_2O_3-GNP and from the wear track of the tested sample. SEM images of the locations where the lamellae were acquired are included in the supportive information (SI), see Fig. S1. The lamellae used for STXM analysis at the Al K-edge were fabricated using a FEI Versa 3D with a Ga^+ ion source. To avoid changes in the structure of the GNP due to Ga^+ implantation, a Thermo Scientific Helios 5 PFIB UXe DualBeam Plasma FIB with a Xe^+ source was used for the lamellae to be analyzed at the C K- edge.

STXM analyses were performed at the SoftiMAX beamline at MAXIV and at the SpectroMicroscopy beamline (10ID1) at the Canadian Light Source (CLS). Linear dichroism analyses at the C K-edge were performed at the CLS. The orientation of the E-vector was rotated from 0° to +90° by changing the position of the girders in the elliptically polarized undulator [23]. The STXM data was analyzed using aXis2000 [24]. In brief, image sequences (stacks) measured at the Al and C K-edge were aligned and converted to optical density (OD) using as Io the signal from off of the FIB section. The Al K-edge was measured from 1540 to 1610 eV and the C K-edge was measured from 278 to 320 eV. Two data analysis procedures were used – forward fitting (also known as linear combination fitting, LCF) and multivariate statistical analysis (MSA). In the forward fitting approach, spectra of regions with characteristic energy- or polarization-dependent contrast were extracted from the stack. Typically 3–5 regions could be identified by watching a play-back of the stack. These spectra were then used to fit the spectrum at each pixel, using the singular value decomposition (SVD) algorithm [25]. The results of the fit are maps of the chemically or dichroically distinct components. In order to visualize the spatial relationship of the component maps, RGB color coded composites are used. In the multivariate statistical analysis approach [26], the stack is subjected to a principle component analysis and then these components are converted to XANES spectra by a process of clustering. The MSA analysis was executed in this work using the PCA_GUI program (C. Jacobsen, 2012), which is available in the aXis2000 package [24]. In this study, we found applying both approaches gave a more meaningful analysis than using just one or the other. Visualization of the MSA results is also aided using RGB color coded composites of the cluster components. Further details of STXM data analysis procedures are given elsewhere [24,27].

A Leo 1550 Gemini SEM with field emission gun was used to image the polished cross-section samples. High resolution TEM imaging and chemical analyses using energy dispersive X-ray analysis (EDS) were performed in a FEI Titan 80–300 operated at 300 keV. For processing and standardless quantification of EDS data, the TIA (TEM Imaging and Analysis) software was used. The background was removed from the spectra through a digital filtering algorithm, whereby the background is convoluted with a "top-hat" filter. In the standardless quantification procedure, the peaks are fit to theoretical Gaussian peaks and the integrated peak intensity is calculated. The integrated intensity is then used along with the Cliff-Lorimer k-factors and a thin-foil absorption correction to calculate the elemental composition [28].

Dry-sliding wear tests on the SPS Al_2O_3 coating and on the bulk alumina sample were performed using a Ball-on-Disc tribometer (TRB3, Anton-Paar, Netherlands). An alumina ball of 6 mm diameter (ST instruments B.V., Netherlands) was used as the counter surface. For the SPS Al_2O_3 coating the test was performed with a normal load of 5 N, the

linear speed was kept at 0.2 m/s and the sliding distance was 2000 m. For the bulk alumina sample a load of 30 N was used.

3. Results and discussion

3.1. STXM at Al K-edge

STXM data at the Al K-edge were obtained by scanning the samples with the X-ray beam perpendicular to the FIB lamellae. Fig. 1 shows Al K-edge X-ray Absorption Near Edge Spectroscopy (XANES) spectra extracted from an Al K-edge stack measured on the as-sprayed sample. Component maps were obtained by SVD fitting the STXM image stack with the XANES spectra shown in Fig. 1. Fig. 2 shows the individual component maps in gray scale and a color composite of the component maps. As depicted in Fig. 1, the obtained absorption spectra for the as-sprayed Al_2O_3 sample reveals three different alumina components: α-alumina, γ-alumina and amorphous alumina [29]. The presence of such phases is commonly reported for SPS alumina coatings [30]. The most prominent spectrum can be attributed to α-alumina, as confirmed by the presence of pronounced peaks of Al^{3+} in octahedral coordination at 1567.6(3) and 1571.6(3) eV [31]. These features are directly associated with the coordination of oxygen atoms in the structure of aluminum (Al) oxides. Aluminum atoms can be coordinated with four or six oxygen atoms in different crystal structures that can co-exist in many aluminum oxide compounds [31]. The presence of γ-alumina is supported by the weak peak around 1565.4(3) which can be attributed to the AlO_4 tetrahedral coordination present in γ-alumina [29,32]. The component maps derived by the SVD fitting procedure (Fig. 2) highlight the spatial distribution of each phase in the sample.

One of the challenges of forward fitting analysis is identifying the correct number of components to include in the SVD fitting. To assist in this the PCA_GUI routine (Jacobsen version 2012) [26] was used to (i) identify the number of statistically significant spectral components, and (ii) derive estimates of the correct spectra and spatial distributions of these components. The PCA_GUI results for both the as-made and wear-tested Al K-edge stacks are included as SI in Figs. S2 and S6.

An additional SVD fitting with five spectral components directly extracted from discontinuous areas in the sample was also performed. However, three of these spectra have only minor differences and all three can be associated with α-alumina. Since the spatial distribution of the different phases is already clearly highlighted by the fitting provided in Fig. 2, the results from this analysis are only included as supportive information in Figs. S3 and S4.

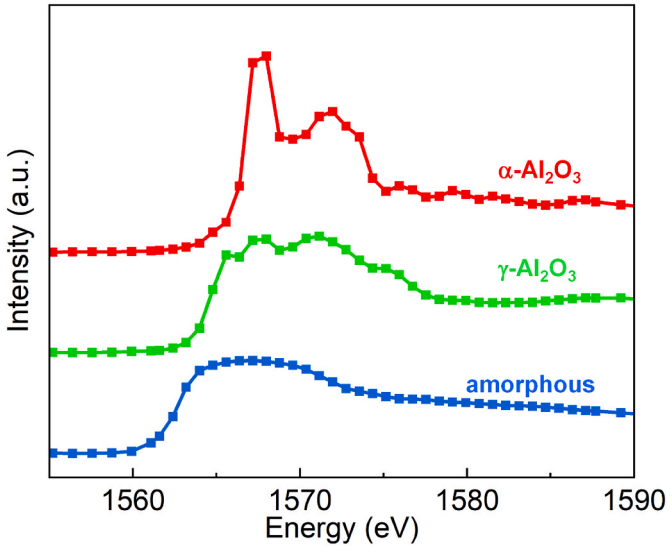

Fig. 1. Al K-edge XANES spectra measured for the as-sprayed Al_2O_3-GNP sample. (A colour version of this figure can be viewed online.)

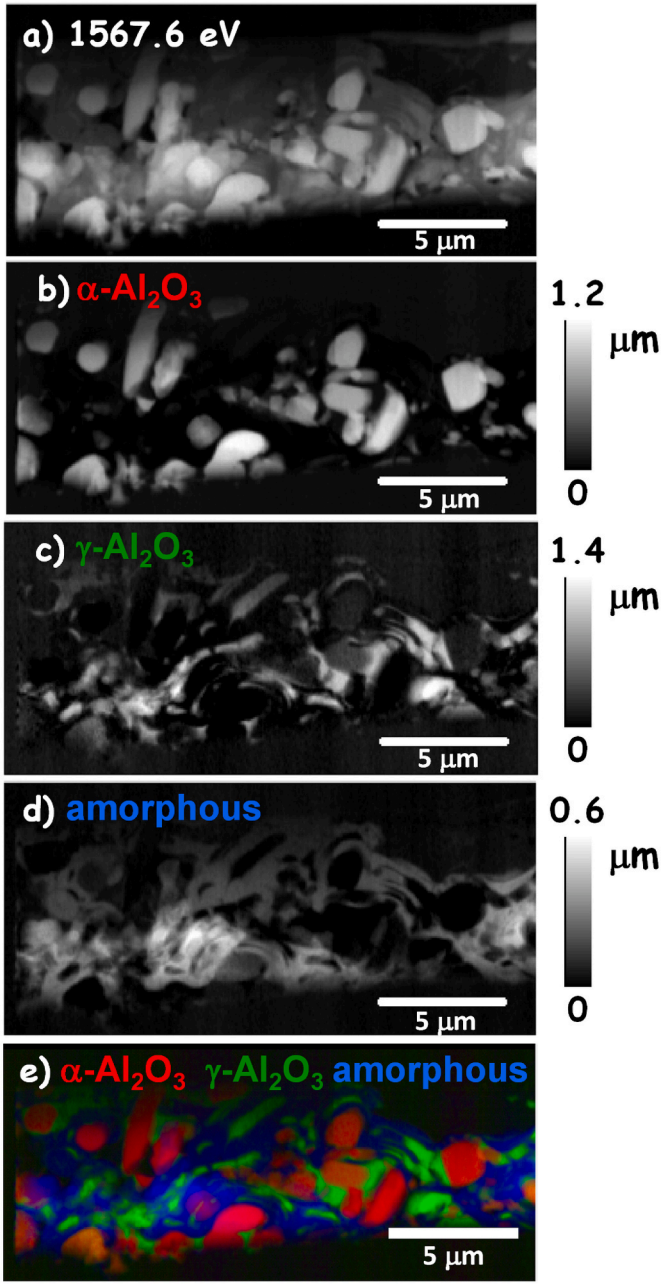

Fig. 2. STXM mapping at the Al K-edge of the as-sprayed Al_2O_3-GNP sample. (a) optical density image at 1567.6 eV (peak of α-Al_2O_3 signal [31]). (b–d) component maps of α-Al_2O_3 (b), γ-Al_2O_3 (c), and (d) amorphous-Al_2O_3 are shown in gray scale. (e) Color coded composite map of the α-Al_2O_3 (red), γ-Al_2O_3 (green) and amorphous-Al_2O_3 (blue). The 0–255 color intensity scale has been matched to full range of each component map. (A colour version of this figure can be viewed online.)

Fig. 3 presents the SVD fitting analysis of the Al K stack measured from the wear-tested sample, whereas the Al K-edge XANES spectra are shown in Fig. 4. As shown in Fig. 3c, amorphous alumina is found to have formed in the first few micrometers below the surface of the sample. Large grains of α-Al_2O_3 are only observed in the lower part of the lamella whereas small α-Al_2O_3 grains, mostly less than one μm in size, are distributed in the amorphous layer (Fig. 3b). As shown in Fig. 4, the spectrum associated with the amorphous alumina phase still contains weak structural spectral components of the α-alumina phase, i.e. small peaks at 1567.6(3) and 1571.6(3) eV. This explains why some of

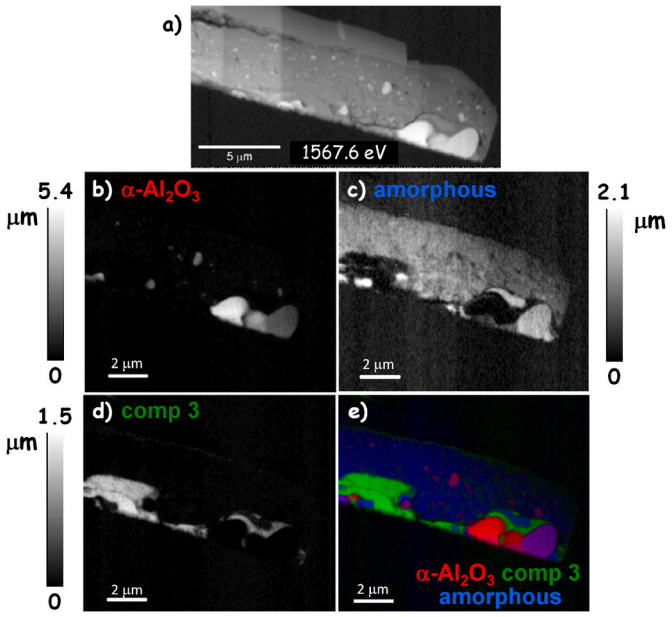

Fig. 3. STXM mapping at the Al K-edge of the wear-tested Al_2O_3-GNP sample shown in an optical density image (a) acquired at 1567.6 eV. The component maps of the different phases are shown in gray scale (b–d), whereas the composite map is shown in color (e). (A colour version of this figure can be viewed online.)

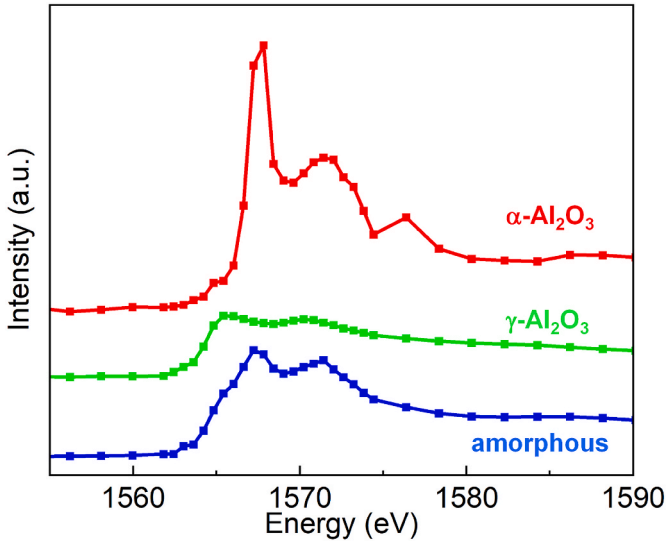

Fig. 4. Al K-edge XANES spectra measured for the wear-tested Al_2O_3-GNP sample. (A colour version of this figure can be viewed online.)

the large α-alumina grains in the lower part of the lamella are also shown with a relatively high intensity on the amorphous component map in Fig. 3c. The presence of such α-alumina spectral components in the amorphous phase represents a confirmation that such amorphous phase has formed as a consequence of the high deformation/pressure occurring in the material during wear testing: the high forces cause an increase in the structural disorder of α-alumina phase leading to its transformation into an amorphous phase. To the best of the authors knowledge, the formation of an amorphous layer after wear testing of SPS Al_2O_3 coatings has not been reported before. TEM analysis, discussed in section 3.3, was performed on the wear-tested sample to confirm the amorphous nature of the alumina phase.

Interestingly, γ-alumina grains or spectral components are not found within the amorphous alumina layer. This can be explained by consideration of the lower hardness of γ-alumina as compared to α-alumina (i.e., ~17 and 22 GPa, respectively [33,34]), resulting in a faster amorphization of the γ-alumina phase. The spectrum of component 3, shown in Fig. 3d, highly resembles the reference γ-alumina spectrum acquired from the as-deposited sample, see Fig. 1. However, the two spectra are characterized by distinctive differences, as shown in Fig. S5 of the SI. Component 3 can be associated to a deformed aluminum oxide phase, as previously reported in another study [35]. Therefore, it is reasonable to assume that component 3 is related to the deformation of gamma phase occurring due to the wear testing.

As for the as-sprayed sample, PCA_GUI analysis was performed on the Al K-edge stack of the wear tested sample in order to identify the number of statistically distinguishable spectra components, as with the results for the as-made sample, the PCA_GUI analysis of the wear tested sample identified 5 components, but only 3 were alumina. The PCA_GUI results are included in Fig. S6 while Figs. S7 and S8 shows an additional SVD fitting with five spectral components directly extracted from discontinuous areas in the sample.

3.2. STXM at the C K-edge

STXM data at the C K-edge were obtained from the as-sprayed sample and are shown in Fig. 5. Linear dichroism measurements included in Fig. 6 were performed by rotating the E vector of the X-ray beam 90°, i.e., from linear horizontal (LH) to linear vertical (LV), to determine the orientation of the GNP [36]. The area from where the data were collected is highlighted with a red dashed box in the SEM micrograph in Fig. 5a. Fig. 5b and **c** show the individual component maps in gray scale and a color composite map for the data acquired with LH and LV illumination, respectively. The representative XANES spectra for each component are shown in Fig. 6. As can be seen, the graphitic planar structure of the GNP is preserved after the SPS process, as evidenced by the presence of peaks at 285.6 eV and 292 eV in Fig. 6, corresponding to excitation of π and σ orbitals [17]. There is no evidence for C in the alumina matrix, as shown by the absence of any peaks in the C K-edge spectra acquired from the matrix regions (see Fig. 6). The C K-edge spectral changes, particularly at 285 and 292 eV, upon rotation of the E vector from LH to LV, indicating strong linear dichroism of the GNP. The same area of scanned GNP shows a strong σ* (292 eV) resonance intensity under LH illumination and a strong π* (285 eV) resonance intensity under LV illumination, as seen in the composite maps in Fig. 5 and the spectra in Fig. 6. This finding is of particular importance since it confirms that the graphene platelets are aligned parallel to the surface of the alumina-GNP composite. With the GNP aligned parallel to the surface, the sliding of the 2D graphitic planes can occur during the wear test resulting in GNP-assisted solid lubrication [37].

It is worth mentioning that a diagonal striped pattern is visible in Fig. 5d and e. These stripes are a moiré artefact caused by beating of the scanning frequency and a modulation of the incident intensity and/or photon energy associated with vibrational motion of one or more of the beamline optics and/or the trajectory of the electron beam in the CLS storage ring. The phenomenon is intermittent, not well understood, and difficult to correct. As the images included in Fig. S9 indicate, the moiré pattern is strongest below the onset of C 1s absorption (280–284 eV). This is the energy region where absorption by the alumina is strongest, so that is why the moiré signal is strongest in the Al_2O_3 map (see Fig. 5d and **h**).

STXM data at the C K edge was also acquired from the wear tested sample and the results are shown in Fig. 7. As shown in the color composite map in Fig. 7b, the presence of GNP (highlighted with white arrows in Fig. 7b) can be observed mainly at the surface of the wear track, i.e. just below the W protective layer. A few GNP can also be observed within the amorphous alumina layer, highlighted with dashed white arrows in Fig. 7b. Peaks corresponding to both π* and σ* resonances are found at 285 eV and 292 eV in the spectrum of the GNP, see Fig. 7c. The

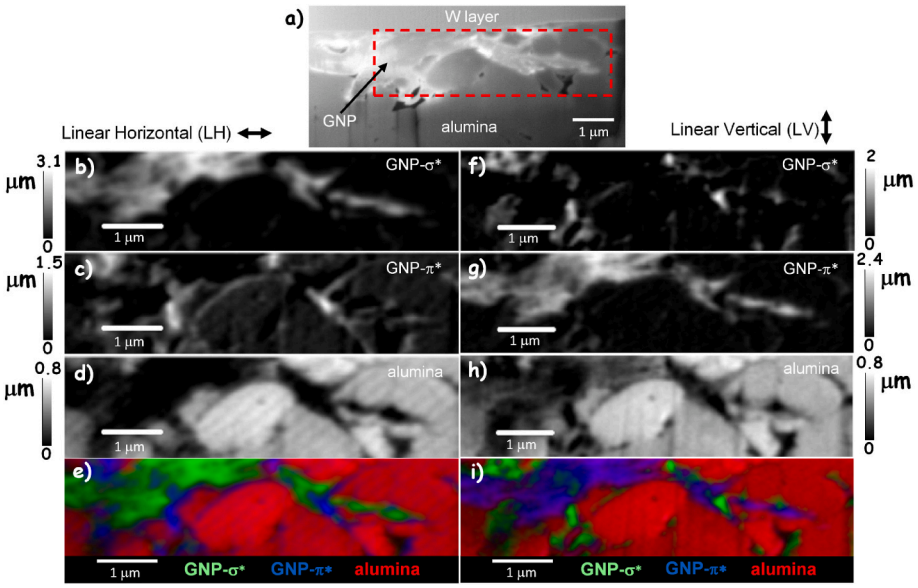

Fig. 5. STXM mapping at the C–K edge of the as-sprayed Al_2O_3-GNP sample shown in the SEM micrograph in (a). The red dashed box in (a) marks the area that was scanned with the X-ray beam. Data acquired with linear horizontal (LH) polarization are shown in (b–e) while data acquired with linear vertical (LV) illumination are shown in (f–i). (A colour version of this figure can be viewed online.)

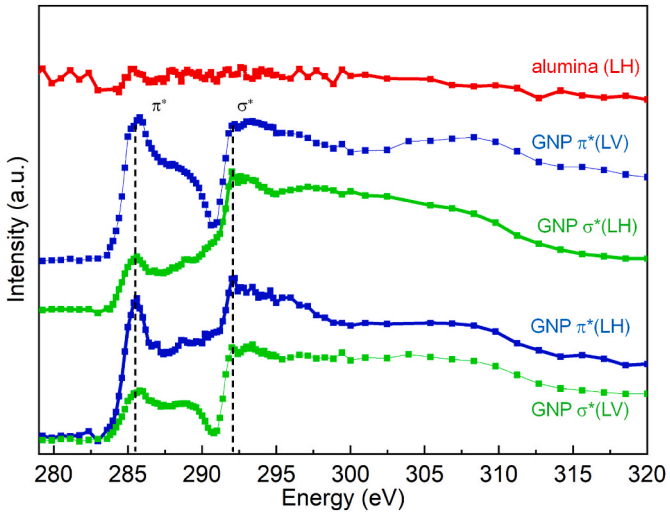

Fig. 6. C K-edge XANES spectra of the as-sprayed Al_2O_3-GNP sample measured with linear horizontal (LH) and linear vertical (LV) polarized X-rays. (A colour version of this figure can be viewed online.)

presence of the GNP forming a tribolayer during the wear test, together with the results showing that the GNP in the as-sprayed sample are aligned parallel to the surface, can convincingly explain the improved wear performance observed for the Al_2O_3-GNP composite. In fact, as shown in our previous study describing the wear behavior of the Al_2O_3-GNP coatings, a 36 % reduction in the coefficient of friction and a 69 % reduction in the wear rate were observed for the Al_2O_3-GNP coating compared to the monolithic alumina coating [7]. The results of the wear tested sample also show that the spectra acquired from the amorphous alumina layer are characterized by a sharp and intense peak at 290.3 eV. This peak can be related to an amorphous carbonate [38] dissolved in the amorphous alumina. Amorphization of GNP in a dry sliding wear test was previously reported by Derelizade et al. [39]. The high forces and the heat generated by the contact between the sliding surfaces can lead to oxidation and an increase in the structural disorder of the GNP. As the wear test progresses, the increase in such structural disorder leads to the amorphization of the GNP. It can be assumed that the amorphization of the alumina matrix and the GNP occur simultaneously and that the carbon diffuses into the alumina, as shown in the results in Fig. 7. Wear tests were also carried out on thermally sprayed pure alumina samples (without GNP) and on sintered bulk alumina samples to investigate the role of GNP and porosity in alumina amorphization by means of SEM analysis on the cross-sections of the tested samples. The results are presented in Figs. 9 and 10 in the next paragraph. To confirm the amorphous nature of the aluminum oxide after the wear test, high-resolution TEM imaging was carried out. Additionally, STEM-EDX analysis was performed to confirm the presence of carbon in the amorphous alumina. The results are described in the following section.

3.3. TEM, STEM-EDS, and SEM analysis

The TEM imaging results of the wear tested sample are shown in Fig. 8, while the STEM-EDS results are summarized in Table 1. In the microscopic image in Fig. 8a, the main components of the lamella can be clearly identified, i.e., (i) the Pt layer, (ii) the amorphous alumina layer, (iii) crystalline alumina grains. The high-resolution image shown in Fig. 8b is acquired from the amorphous alumina layer and from the area in Fig. 8a highlighted with a white box. The amorphous alumina layer and its amorphous nature is confirmed by the Fast Fourier Transform (FFT) acquired from the area highlighted in turquoise in Fig. 8b where no diffraction spots can be observed. However, the area below the wear track is not homogeneously amorphous: submicron and nanometre-sized alumina grains are distributed within the amorphous layer. Some larger grains are marked with an arrow in Fig. 8a, a nanometric grain is shown in Fig. 8b in the area highlighted in green and its corresponding FFT shows diffraction spots. STEM-EDS analysis was carried out to determine the presence of carbon in the amorphous alumina and the bulk crystalline alumina, e.g. at point 1 and 2 in Fig. 8a, respectively. The measured average composition is given in Table 1. The measured carbon content appears to be high in both the amorphous and crystalline alumina. Contamination of the lamella during the handling of the TEM half grid holder could partially explain the C signal. The significant difference in C content in the amorphous alumina, i.e., four times higher compared to the bulk alumina, confirms the synchrotron results (Fig. 8) and the hypothesis that carbon dissolves in the amorphous alumina during the wear test.

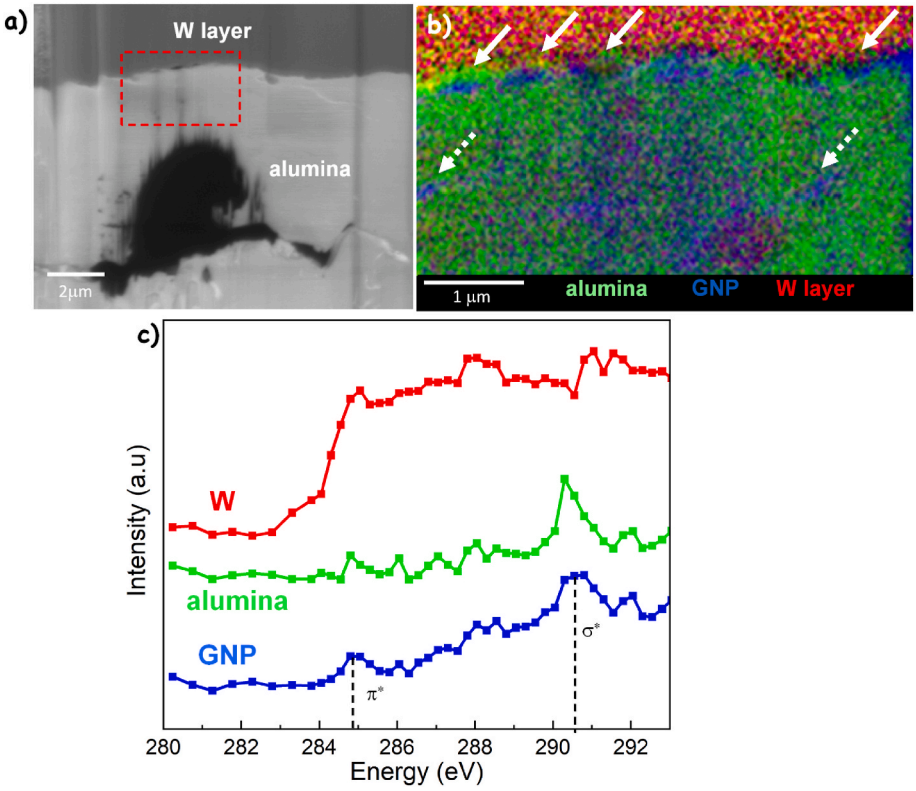

Fig. 7. STXM mapping at the C–K edge of the wear-tested Al_2O_3-GNP sample shown in the SEM micrograph in (a). The red dashed box in (a) marks the area of the sample that was scanned with the X-ray beam. The obtained color composite map and acquired XANES spectra are shown in (b) and in (c), respectively. (A colour version of this figure can be viewed online.)

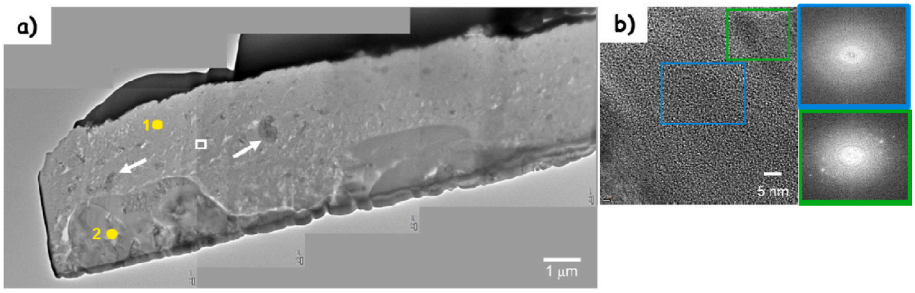

Fig. 8. TEM micrograph of wear tested sample (a). Points 1 and 2 in the micrograph mark the amorphous and crystalline region where the STEM-EDS point spectra were acquired. (b) High resolution TEM micrograph acquired from the amorphous alumina layer with FFTs, confirming the amorphous structure and the presence of crystalline grains in the layer. The white square in (a) highlights the area from where the high-resolution TEM micrograph was acquired. (A colour version of this figure can be viewed online.)

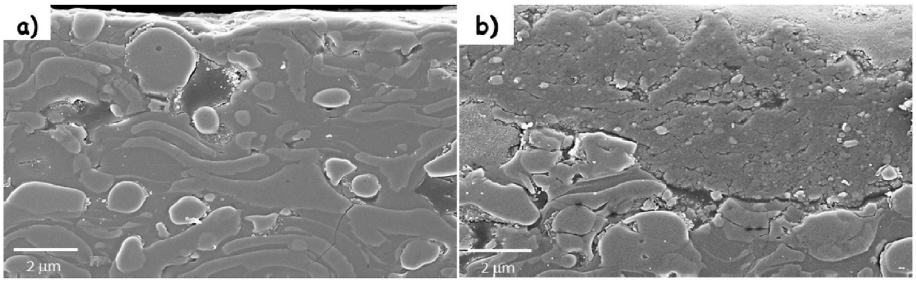

Fig. 9. Cross-section SEM micrographs of the Al_2O_3-GNP sample acquired from a wear-free area (a) and from the area below the wear track (b). (A colour version of this figure can be viewed online.)

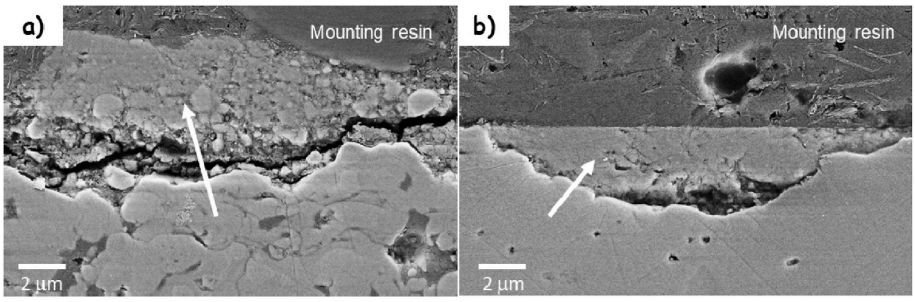

Fig. 10. Cross-section SEM micrographs of the wear track of a SPS Al_2O_3 coating (a) and of a bulk alumina sample (b). The white arrows in the micrographs highlight the presence of highly deformed alumina. (A colour version of this figure can be viewed online.)

Table 1
Chemical composition measured with STEM-EDS point analysis. Points 1 and 2 refer to the locations shown in Fig. 8.

Point	Al (wt.%)	O (wt.%)	C (wt.%)
1	27 ± 2	19 ± 2	54 ± 2
2	53 ± 4	34 ± 2	13 ± 2

To confirm the reproducibility of the results regarding the formation of an amorphous layer after the wear test, SEM images were taken of the polished cross section of the wear-tested sample to compare the microstructure under the wear track with the wear-free microstructure. As can be seen in Fig. 9, the cross section of the area not affected by the wear test (Fig. 9a) is very different from the area under the wear track (Fig. 9b) and has clearly visible alumina grains up to the sample surface. In Fig. 9b a clearly deformed (amorphous) alumina layer can be observed in the area of the wear track.

Wear tests were also carried out on thermally sprayed (SPS) pure alumina samples (without GNP) and on sintered bulk alumina samples to investigate the role of GNP and porosity in alumina amorphization. The same test parameters were used as in the previous work [7]. The cross-section SEM micrographs acquired from the area below the wear tracks are shown in Fig. 10. As can be seen, in both cases (Fig. 10a and **b**), the alumina is deformed in the area of the wear track. This means that the appearance of amorphous alumina during the wear test cannot be ascribed to either porosity or the presence of GNP.

4. Summary

In this study, SPS Al_2O_3-GNP coatings, produced for improved tribological performance, were characterized by synchrotron STXM. The aim was to locate the GNP and reveal their orientation in both the as-sprayed host matrix and in the wear track, in order to reveal the transformations that occur in the graphene platelets and the host alumina matrix during wear tests. To complement the synchrotron measurements, high resolution TEM, STEM-EDS and SEM analyses were performed. From the obtained results the following conclusions were drawn:

- STXM data collected at the Al K-edge show that the as-sprayed sample consists of three different phases: α, γ, and amorphous alumina. Wear tests result in the formation of a ~3 µm layer of amorphous alumina with submicron α-Al_2O_3 grains distributed throughout the layer.
- STXM data acquired at the C K-edge shows that the GNP are well preserved in the as-sprayed alumina matrix. As shown by the linear dichroism results, the graphene platelets are aligned parallel to the sample surface. After wear testing, GNP are mainly found at the tribosurface of the Al_2O_3-GNP coating. These results provide a clear explanation of the improvement in the wear resistance observed in the composite coatings.
- After the wear test, amorphous carbon is distributed within the amorphous alumina layer. This is also confirmed by TEM and STEM-EDS analysis, which show that there is a significantly higher wt.% of C in the amorphous alumina, as compared to the crystalline alumina. The formation of these amorphous phases is believed to occur simultaneously due to the high forces generated during wear testing.
- The results of the wear tests on the GNP-free SPS Al_2O_3 coating and on the sintered alumina sample showed that neither porosity nor the presence of GNP can be held responsible for the appearance of amorphous alumina during the wear test.

CRediT authorship contribution statement

Antonio Mulone: Writing – original draft, Visualization, Investigation, Data curation. **Plinio Fernandes Borges Silva:** Writing – review & editing, Investigation, Data curation. **Hui Yuan:** Writing – review & editing, Resources. **Karina Thånell:** Writing – review & editing, Resources, Investigation. **Adam Hitchcock:** Writing – review & editing, Visualization, Validation, Software, Methodology, Investigation, Formal analysis, Data curation. **Uta Klement:** Writing – review & editing, Validation, Supervision, Project administration, Methodology, Investigation, Funding acquisition, Conceptualization.

Declaration of competing interest

The authors declare that they have no known competing financial interests or personal relationships that could have appeared to influence the work reported in this paper.

Acknowledgements

We acknowledge MAX IV Laboratory for time on the SoftiMAX Beamline under Proposal ID 20210987 and 20221143. Research conducted at MAX IV, a Swedish national user facility, is supported by the Swedish Research Council under contract 2018–07152 and 2020–06159, the Swedish Governmental Agency for Innovation Systems under contract 2018–04969, and Formas under contract 2019–02496.

Measurements were also made at the ambient STXM on the SpectroMicroscopy beamline 10ID1 at the CLS. CLS is funded by the Canada Foundation for Innovation (CFI), the Natural Sciences and Engineering Research Council (NSERC), the National Research Council (NRC), the Canadian Institute for Health Research (CIHR), the Government of Saskatchewan, and the University of Saskatchewan. We thank the beamline staff at CLS-SM (Jian Wang). The spraying of the alumina-GNP samples was performed at University West, Trollhättan, Sweden, in a project financed by the national Strategic Innovation Programme for graphene, SIO Grafen, under the contract number 2018–03315. Focused ion beam (FIB) sample preparation was performed at the Canadian Centre for Electron Microscopy (CCEM) which is funded by CFI, and at the Chalmers Materials Analysis Laboratory (CMAL). The high-resolution TEM investigation was performed at CMAL with the help of

Dr. Ludvig de Knoop. We thank Prof. Shrikant Joshi and Dr. Kaveh Torkashvand (University West, Trollhättan, Sweden) for helping with the wear measurements on the pure alumina sample. The participation of UK, AM, and PFBS was supported by the Chalmers Foundation. The participation of APH in the research was supported by NSERC Discovery Grant program.

Appendix A. Supplementary data

Supplementary data to this article can be found online at https://doi.org/10.1016/j.carbon.2024.119245.

References

[1] D.G. Papageorgiou, I.A. Kinloch, R.J. Young, Mechanical properties of graphene and graphene-based nanocomposites, Prog. Mater. Sci. 90 (2017) 75–127, https://doi.org/10.1016/J.PMATSCI.2017.07.004.
[2] D. Berman, A. Erdemir, A.V. Sumant, Graphene: a new emerging lubricant, Mater. Today 17 (2014) 31–42, https://doi.org/10.1016/j.mattod.2013.12.003.
[3] S. Zhou, Y. Wu, W. Zhao, J. Yu, F. Jiang, Y. Wu, L. Ma, Designing reduced graphene oxide/zinc rich epoxy composite coatings for improving the anticorrosion performance of carbon steel substrate, Mater. Des. 169 (2019) 107694, https://doi.org/10.1016/j.matdes.2019.107694.
[4] Y. Liu, X. Ge, J. Li, Graphene lubrication, Appl. Mater. Today 20 (2020).
[5] K. Markandan, J.K. Chin, M.T.T. Tan, Recent Progress in Graphene Based Ceramic Composites : a Review, 2016, https://doi.org/10.1557/jmr.2016.390.
[6] A. Mulone, S. Mahade, S. Björklund, D. Lundström, B. Kjellman, S. Joshi, U. Klement, Development of yttria-stabilized zirconia and graphene coatings obtained by suspension plasma spraying: thermal stability and influence on mechanical properties, Ceram. Int. (2022), https://doi.org/10.1016/j.ceramint.2022.11.055.
[7] S. Mahade, A. Mulone, S. Björklund, U. Klement, S. Joshi, Incorporation of graphene nano platelets in suspension plasma sprayed alumina coatings for improved tribological properties, Appl. Surf. Sci. 570 (2021) 151227, https://doi.org/10.1016/J.APSUSC.2021.151227.
[8] J. Shrikant, P. Nylén, Advanced coatings by thermal spray processes, Technologies 7 (2019), https://doi.org/10.3390/technologies7040079.
[9] J. Fazilleau, C. Delbos, V. Rat, J.F. Coudert, P. Fauchais, B. Pateyron, Phenomena involved in suspension plasma spraying Part 1: suspension injection and behavior, Plasma Chem. Plasma Process. 26 (2006) 371–391.
[10] J.W. Murray, G.A. Rance, F. Xu, T. Hussain, Alumina-graphene nanocomposite coatings fabricated by suspension high velocity oxy-fuel thermal spraying for ultra-low-wear, J. Eur. Ceram. Soc. 38 (2018) 1819–1828, https://doi.org/10.1016/j.jeurceramsoc.2017.10.022.
[11] B. Mukherjee, O.S. Asiq Rahman, A. Islam, M. Sribalaji, A.K. Keshri, Plasma sprayed carbon nanotube and graphene nanoplatelets reinforced alumina hybrid composite coating with outstanding toughness, J. Alloys Compd. 727 (2017) 658–670, https://doi.org/10.1016/j.jallcom.2017.08.160.
[12] X. Li, S. Liu, M. Qiu, Scanning probe microscopy of topological structure induced electronic states of graphene, Small Methods 4 (2020), https://doi.org/10.1002/smtd.201900683.
[13] A. Mulone, S. Mahade, S. Björklund, D. Lundström, B. Kjellman, S. Joshi, U. Klement, Development of yttria-stabilized zirconia and graphene coatings obtained by suspension plasma spraying: thermal stability and influence on mechanical properties, Ceram. Int. (2022), https://doi.org/10.1016/J.CERAMINT.2022.11.055.
[14] J. Hicks, E.H. Conrad, Graphene investigated by synchrotron radiation, MRS Bull. 37 (2012) 1203–1213, https://doi.org/10.1557/mrs.2012.236.
[15] Y. Ding, H. Shi, M. Zeng, L. Fu, Exploring interface through synchrotron radiation characterization techniques: a graphene case, Adv. Funct. Mater. 2202469 (2022) 1–19, https://doi.org/10.1002/adfm.202202469.
[16] W. Wang, Y. Wang, R. He, X. Wang, Z. Shen, X. Han, A. Bachmatiuk, W. Wen, M. H. Rümmeli, P. Liu, M. Zeng, L. Fu, Ultrafast single-crystal-to-single-crystal transformation from metal–organic framework to 2D hydroxide, Adv. Mater. 34 (2022).
[17] S.J. Rezvani, A. D'Elia, S. Macis, S. Nannarone, S. Lupi, F. Schütt, F. Rasch, R. Adelung, B. Lu, Z. Zhang, L. Qu, X. Feng, A.R. Vázquez, A. Marcelli, Structural anisotropy in three dimensional macroporous graphene: a polarized XANES investigation, Diam. Relat. Mater. 111 (2021) 108171, https://doi.org/10.1016/J.DIAMOND.2020.108171.
[18] J. Stöhr, NEXAFS Spectroscopy, 25th ed., Springer Tracts in Surface Science, 1992.
[19] A.P. Hitchcock, Soft X-ray spectromicroscopy and ptychography, J. Electron. Spectrosc. Relat. Phenom. 200 (2015) 49–63, https://doi.org/10.1016/j.elspec.2015.05.013.
[20] C. Jacobsen, X-Ray Microscopy, Cambridge University Press, 2019.
[21] A.P. Hitchcock, Soft X-ray imaging and spectromicroscopy chapter 22, in: Gustaaf Van Tendeloo, Dirk Van Dyck, Stephen J. Pennycook (Eds.), Volume II of the Handbook on Nanoscopy, Wiley, 2012, pp. 745–791.
[22] H. Jun, C. Dindault, D. Tondelier, B. Geffroy, I. Florea, J.E. Bouree, P. Schulz, Y. Bonnassieux, S. Swaraj, On the use of soft X-ray STXM for organic-inorganic halide perovskite photovoltaic materials, J. Electron. Spectrosc. Relat. Phenom. 266 (2023), https://doi.org/10.1016/j.elspec.2023.147358.
[23] A.T. Young, E. Arenholz, S. Marks, R. Schlueter, C. Steier, H.A. Padmore, A. P. Hitchcock, D.G. Castner, Variable linear polarization from an X-ray undulator, J. Synchrotron Radiat. 9 (2002) 270–274.
[24] A.P. Hitchcock, Analysis of X-ray Images and Spectra (aXis2000): a toolkit for the analysis of X-ray spectromicroscopy data, J. Electron. Spectrosc. Relat. Phenom. 266 (2023) 147360.
[25] I.N. Koprinarov, A.P. Hitchcock, C. McCrory, R.F. Childs, Quantitative mapping of structured polymeric systems using singular value decomposition analysis of soft X-ray images, J. Phys. Chem. B 106 (2002) 5358–5364.
[26] M. Lerotic, C. Jacobsen, J.B. Gillow, A.J. Francis, S. Wirick, S. Vogt, J. Maser, Cluster analysis in soft X-ray spectromicroscopy: finding the patterns in complex specimens, J. El. Spec. Rel. Phen. 144 (2005) 1137.
[27] M.A. Marcus, Data analysis in spectroscopic STXM, J. Electron. Spectrosc. Relat. Phenom. 264 (2023) 147310, https://doi.org/10.1016/j.elspec.2023.147310.
[28] A. Mulone, I. Ennen, A. Hütten, U. Klement, In-situ TEM annealing of amorphous Fe-24at.%W coatings and the effect of crystallization on hardness, J. Mater. Sci. (2020), https://doi.org/10.1007/s10853-020-05485-7.
[29] T. Yamamoto, T. Kudo, T. Yamamoto, J. Kawai, Analysis of coordination environment of aluminum species in zeolites and amorphous silica-alumina by X-ray absorption and emission spectroscopy, Microporous Mesoporous Mater. 182 (2013) 239–243, https://doi.org/10.1016/j.micromeso.2013.03.047.
[30] J.W. Murray, A.S.M. Ang, Z. Pala, E.C. Shaw, T. Hussain, Suspension high velocity oxy-fuel (SHVOF)-Sprayed alumina coatings: microstructure, nanoindentation and wear, J. Therm. Spray Technol. 25 (2016) 1700–1710, https://doi.org/10.1007/s11666-016-0462-0.
[31] D. Cabaret, P. Sainctavit, P. Ildefonse, A.-M. Flank, Full multiple-scattering calculations on silicates and oxides at the Al K edge, J. Phys. Condens. Matter 8 (1996) 3691–3704, https://doi.org/10.1088/0953-8984/8/20/015.
[32] Y. Kato, K. Shimizu, N. Matsushita, T. Yoshida, H. Yoshida, A. Satsuma, T. Hattori, Quantification of aluminium coordinations in alumina and silica–alumina by Al K-edge XANES, Phys. Chem. Chem. Phys. 3 (2001) 1925–1929, https://doi.org/10.1039/B100610J.
[33] O. Zywitzki, G. Hoetzsch, Influence of coating parameters on the structure and properties of Al2O3 layers reactively deposited by means of pulsed magnetron sputtering, Surf. Coating. Technol. 86–87 (1996) 640–647, https://doi.org/10.1016/S0257-8972(96)02992-1.
[34] T.M.H. Costa, M.R. Gallas, E.V. Benvenutti, J.A.H. da Jornada, Study of nanocrystalline γ-Al2O3 produced by high-pressure compaction, J. Phys. Chem. B 103 (1999) (1999) 4278–4284.
[35] A.L. Butterworth, A.J. Westphal, T. Tyliszczak, Z. Gainsforth, J. Stodolna, D. R. Frank, C. Allen, D. Anderson, A. Ansari, S. Bajt, R.K. Bastien, N. Bassim, H. A. Bechtel, J. Borg, F.E. Brenker, J. Bridges, D.E. Brownlee, M. Burchell, M. Burghammer, H. Changela, P. Cloetens, A.M. Davis, R. Doll, C. Floss, G. Flynn, E. Grün, P.R. Heck, J.K. Hillier, P. Hoppe, B. Hudson, J. Huth, B. Hvide, A. Kearsley, A.J. King, B. Lai, J. Leitner, L. Lemelle, H. Leroux, A. Leonard, R. Lettieri, W. Marchant, L.R. Nittler, R. Ogliore, W.J. Ong, F. Postberg, M.C. Price, S.A. Sandford, J.A.S. Tresseras, S. Schmitz, T. Schoonjans, G. Silversmit, A. S. Simionovici, V.A. Solé, R. Srama, F.J. Stadermann, T. Stephan, V.J. Sterken, R. M. Stroud, S. Sutton, M. Trieloff, P. Tsou, A. Tsuchiyama, B. Vekemans, L. Vincze, J. Von Korff, N. Wordsworth, D. Zevin, M.E. Zolensky, Stardust interstellar preliminary examination IV: scanning transmission X-ray microscopy analyses of impact features in the Stardust interstellar dust collector, Meteorit. Planet. Sci. 49 (2014) 1562–1593, https://doi.org/10.1111/maps.12220.
[36] E. Najafi, J. Wang, A.P. Hitchcock, J. Guan, S. Dénommée, B. Simard, Characterization of single-walled carbon nanotubes by scanning transmission x-ray spectromicroscopy: purification, order and dodecyl functionalization, J. Am. Chem. Soc. 132 (2010) 9020–9029, https://doi.org/10.1021/ja101001t.
[37] L. Liu, M. Zhou, L. Jin, L. Li, Y. Mo, G. Su, X. Li, H. Zhu, Y. Tian, Recent advances in friction and lubrication of graphene and other 2D materials: mechanisms and applications, Friction 7 (2019) 199–216, https://doi.org/10.1007/s40544-019-0268-4.
[38] Y. Kebukawa, J. Mathurin, E. Dartois, A. Dazzi, A. Deniset-Besseau, J. Duprat, L. Remusat, T. Noguchi, A. Miyake, Y. Igami, M.V. Paoletti, M.E. Zolensky, C. Engrand, C. Sandt, F. Borondics, S. Yamashita, D. Wakabayashi, Y. Takeichi, Y. Takahashi, Complex mixture of organic matter in a xenolithic clast from the Zag meteorite revealed by coordinated analyses using AFM-IR, NanoSIMS and STXM/XANES, Icarus 400 (2023), https://doi.org/10.1016/j.icarus.2023.115582.
[39] K. Derelizade, F. Venturi, R.G. Wellman, A. Khlobystov, T. Hussain, Structural changes of thermal sprayed graphene nano platelets film into amorphous carbon under sliding wear, Appl. Surf. Sci. 528 (2020) 146315, https://doi.org/10.1016/j.apsusc.2020.146315.